

# EFFECT OF END PLATE ON THE FLOW CROSSING A YAWED CIRCULAR CYLINDER

Hui Liang, Sheng-Yao Jiang, and Ri-Qiang Duan\*

Institute of Nuclear and New Energy Technology,  
Collaborative Innovation Center of Advanced Nuclear Energy Technology, Key Laboratory of Advanced  
Reactor Engineering and Safety of Ministry of Education  
Nengke Building, Tsinghua University, Beijing 100084, China  
[liangh13@mails.tsinghua.edu.cn](mailto:liangh13@mails.tsinghua.edu.cn); [jiangshy@tsinghua.edu.cn](mailto:jiangshy@tsinghua.edu.cn); [duanrq@mail.tsinghua.edu.cn](mailto:duanrq@mail.tsinghua.edu.cn)

## ABSTRACT

The uniform flow passing a yawed finite and infinite circular cylinder are numerically investigated in the regime of turbulent vortex street, the study of which is motivated by flow-induced vibration of tube bundle for helically coiled steam generators. The yaw angle of cylinder with flow direction varies from  $0^\circ$  to  $45^\circ$ , and the Reynolds number based on the diameter of cylinder and incoming velocity is taken as 3900. The turbulence behavior in the flow are calculated using Large Eddy Simulation and vortex is captured by *Q-criterion*. We thoroughly examined the flow behavior from the four flow characteristics, i.e. wake vortex structure, streamlines, pressure distribution, and Strouhal number. Our numerical results show that the end plates have a great effect on flow behavior, the wake by which is divided spanwise into three regions, two wall-end regions and the midspan region. In the midspan region, the so-called Independent Principle (IP) is held, which means the flow in this region is still with quasi-two dimension. However, the two wall-end regions exhibit strong different three-dimensional behavior, where the IP is broken down. The inclination of a cylinder induces the vortex concentrated in the downstream wall-end and thus strong shear layer are formed in the downstream wall-end plate.

## KEYWORDS

Inclined circular cylinder, LES, Karman Vortex Street, axial flow, vortex-induced vibration

## 1. INTRODUCTION

Helically coiled steam generators have been utilized extensively in Gas-Cooled Reactors (GCR), such as the Heysham I and Hartlepool advanced GCRs in the UK, the THTR-300 helium-cooled reactor in Germany, the Fort St. Vrain helium-cooled reactor in the USA, and the HTR-10 in China, due to the high efficiency of heat transfer, compactness of structure, and resistance to flow-induced vibration [1]. The shell-side hydrodynamics are typical of flow over yawed circular cylinder bundle. Generally, the Independent principle (hereafter, IP is used) is assumed to be applicable to the estimated vibration frequency of vortex shedding for fluid-tube interaction. The so-called IP means that the characteristics of flow past a yawed infinite cylinder are approximately the same as that of a cylinder with no yaw using only the component of the free-stream flow oriented normal to the cylinder axis.

On the issue of the IP validity, an agreement is not reached up to now, although many experimental and numerical studies have been done. Remberg [2] carried out a series of experiments on a yawed cylinder in wind tunnel, in which the parameters are in a range with  $Re$  from 160 to 1100 and yaw angles from  $-10^\circ$

to  $60^\circ$ . Thakur et al. [3] used flow visualization and particle-image velocimetry to qualify and quantify the velocity and vorticity in the wake region for a yawed cylinder in a water tank. The results of their experiments show that the IP validity is extended up to the yaw angle of  $30^\circ$ . Furthermore, to reveal the spanwise validity of the IP, Hayashi et al. [4, 5] measured the pressure distributions on a yawed circular cylinder surface. Their experimental results showed that quasi-two-dimensional flow is yet held in the middle part except for the two near end-plate regions. They concluded that the failure of the IP is due to the wall effect of the end plates. However, Zhao M. et al. [6], using the direct numerical simulation, attributed the breakdown of the IP to the aspect ratio of the cylinder and their numerical results showed that the IP still holds at  $\alpha = 60^\circ$  for the infinite cases.

From the previous researches, it is found that the boundary condition of end plate has a significant impact on the flow behavior of a yawed cylinder. So in this paper, we try to thoroughly clarify its mechanism, and give further insight of the effect of the end plates. Different boundary conditions are employed at the two end plates of cylinder to investigate the end wall effect at different yaw angles.

## 2. COMPUTATIONAL MODEL

### 2.1. Computational Domain and Boundary Conditions

The computational domain, the coordinate system, and the definition of the cylinder yaw angle  $\alpha$  are depicted in Fig. 1(a). The computational domain is  $35D \times 20D \times 9D$  for flow passing a finite length cylinder and  $35D \times 20D \times 5D$  for infinite cases. The origins of both the global coordinate system ( $Oxyz$ ) and local coordinate system ( $Ox'y'z'$ ) are located at the center point of the circular cylinder axis.

A uniform velocity profile ( $u=U_0, v=w=0$ ) is imposed at the inlet and the streamwise velocity  $U_0$  has a component  $U_N$  normal to the cylinder axis and a component  $U_T$  tangent to the cylinder axis in the inclined cylinder cases (as shown in Fig. 1 (b)). A Neumann boundary condition is used at the outlet boundary. No-slip boundary condition is applied on the surface of the cylinder and a free-slip boundary condition is employed at the two lateral boundaries. At the two end plates of the cylinder, both the free-slip boundary conditions at  $A = 9$  and periodic boundary conditions at  $A = 5$  (which can be seen as  $A = +\infty$ ) are used to investigate the effect of end plate on the characteristics of flow and vibration.

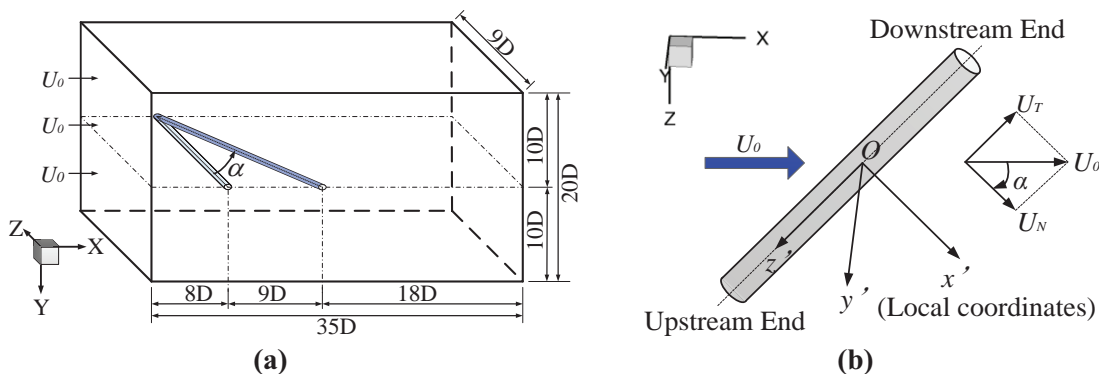


Figure 1. (a) Computational domain for  $\alpha = 45^\circ$ ; (b) Resolution of velocity vector.

### 2.2. Numerical Method

Commercial software, Fluent 15.0, was employed in this study to conduct the simulation. The model was solved by the LES approach with a dynamic Smagorinsky-Lilly subgrid-scale mode which had been

proven to be in better agreement with experiments than those with standard Smagorinsky-Lilly subgrid-scale mode when resolving the flow over a normal circular cylinder [7-9]. A dimensionless time step  $\Delta t U_0/D = 0.02$  was chosen for the present LES, ensuring a sufficiently small CFL number of less than 1 for most parts of the computational domain.

### 2.3. Mesh Independence Test and Validation of Numerical Method

Before extensive simulations for the yawed cases, flow across a stationary circular cylinder at  $\alpha = 0^\circ$  with  $Re = 3900$  is simulated as a benchmark to check the mesh independence and test the suitability of LES. The  $Re$  was taken of 3900 partly for the flow is close to the practical industrial configurations, and partly for the  $Re$  of 3900 case is probably the more documented one in the previous experiments and numerical simulations and can be viewed as a generic benchmark for the subcritical regime.

#### 2.3.1. Mesh independence check

Mesh independence is examined by repeating a three-dimensional flow computation with three different meshing schemes—coarse mesh (387,448 grid points), medium mesh (764,964 grid points), and fine mesh (1,340,496 grid points). The mean drag coefficient  $\bar{C}_D$ , pressure coefficient at the backward stagnation point  $\bar{C}_{pb}$  and the Strouhal Number  $Str$  computed using these three kinds of mesh schemes at  $Re = 3900$  are compared with those of other literature. For the fine mesh,  $\bar{C}_D$  (1.0465) is in the range of measured results between 1.0 and 1.2 [10, 11];  $\bar{C}_{pb}$  is -0.9667, which is smaller than the experimental data between -0.95 and -0.85 [12] but bigger than the previous LES results of -1.049 [8] and -1.06 [13]; and  $Str$  is 0.2082, which is in good agreement with the experimental data between 0.207 and 0.22 [14]. The differences of abovementioned three quantities between the medium mesh and fine mesh are 0.796%, 3.067% and -3.417%, respectively. Therefore, the mesh schemes used in the inclined cases were of the same densities as that of the fine meshing scheme.

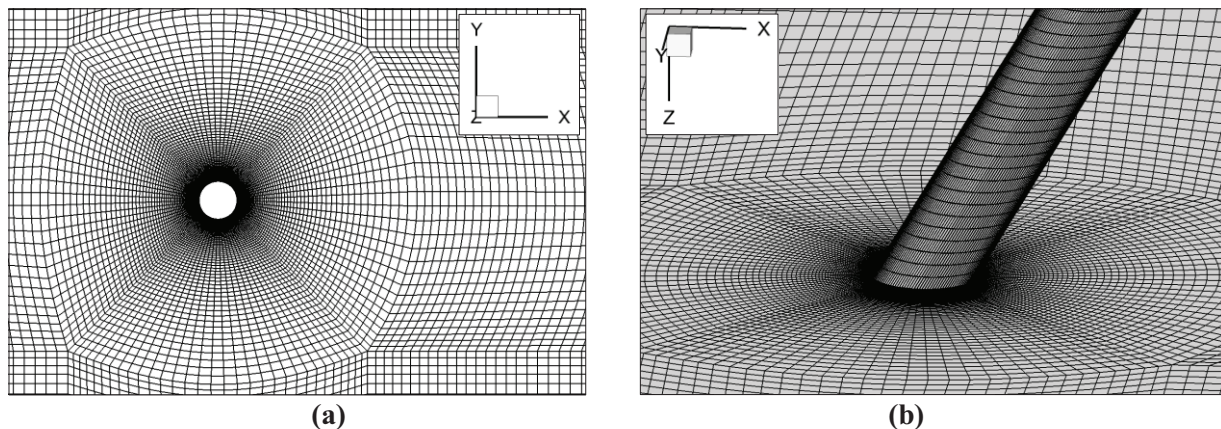


Figure 2. Details of the grid close to the cylinder: (a)  $\alpha = 0^\circ$ ; (b)  $\alpha = 30^\circ$ .

Fig. 2(a, b) show the mesh in the vicinity of the cylinder at  $\alpha = 0^\circ$  and  $\alpha = 30^\circ$  respectively. In these computational domains, a block structured H-grid has been used with an O-grid with radius  $4D$  around the cylinder. The height of the first cell normal to the cylinder surface is chosen to be  $3 \times 10^{-3}D$  to ensure that at least two layers of the nodes next to the cylinder surface are located within  $y^+ < 1$ , which is smaller than the value adopted by Franke & Frank [15] in their LES of the similar cases. The stretching factor of the grid is 1.02 inside of the O-grid while increased to a maximum of 1.05 outside of the O-grid. On the circumference of the cylinder 160 points are used, which is finer than the simulation of Beaudan &

Moin [7] and Franke & Frank [15]. 72 points are used over the spanwise length of  $9D$ , which is a higher spanwise resolution than the simulations of Kawamura & Hayashi [16].

### 2.3.2. Validation of the numerical method

Furthermore, the validation of LES for the flow over a normal circular cylinder was carried out before the extensive simulations.  $\langle u \rangle / U_0$  is the time-averaged streamwise velocity normalized by the free-stream velocity on the centerline in the wake of a circular cylinder over the time period from  $T^* = 180$  to 480. The simulated results of both  $\langle u \rangle / U_0$  (as shown in Fig. 3(a)) and the pressure coefficient  $C_p$  (as shown in Fig. 3(b)) are all in good agreement with previous numerical and experimental data [6, 12, 17-19], which demonstrates the suitability of LES in resolving the flow over a circular cylinder.

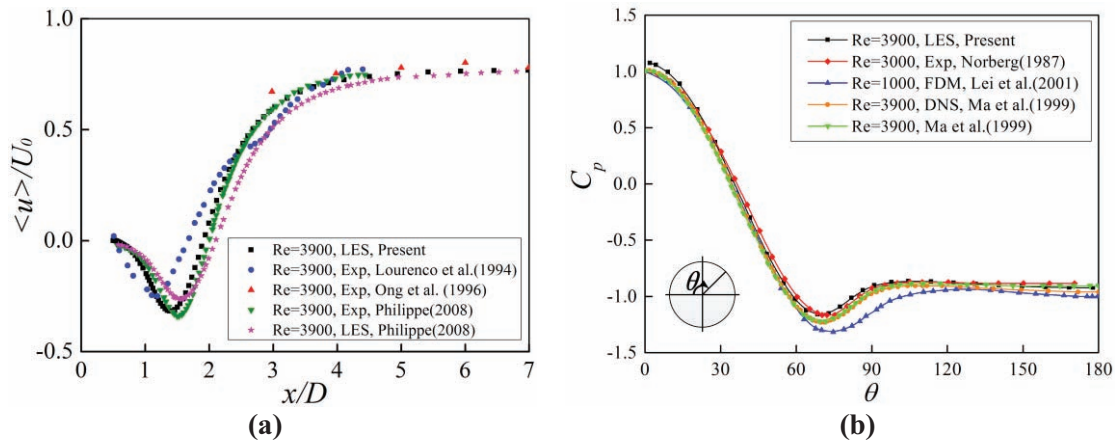


Figure 3: (a) Streamwise velocity normalized by the free-stream velocity on the center line in the wake of a circular cylinder at  $\alpha = 0^\circ$ ; (b) pressure coefficient on the cylinder surface at  $\alpha = 0^\circ$ .

### 2.4. Comparison of Vorticity Magnitude and $Q$ -criterion

Fig. 4 shows the instantaneous vortex flow structures around the circular cylinder at  $A = 9$  and  $T^* = 450$ . The vortex structures are identified by vorticity magnitude  $|\omega|$  and  $Q$ -criterion (the second invariant  $Q$  from the velocity gradient tensor, [20]) respectively.

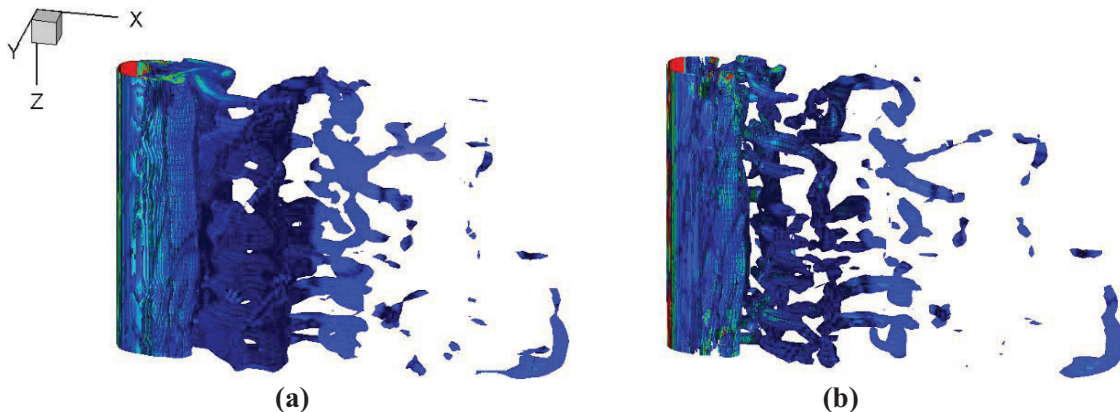


Figure 4. Contours of instantaneous vortex structure for  $\alpha = 0^\circ$ ,  $A=9$  and  $T^*=450$ : (a)  $|\omega| > 50 \text{ s}^{-1}$ ; (b)  $Q = 1000 \text{ s}^{-2}$ .

Fig. 4(a) shows the vortex structure of  $|\omega| > 50 \text{ s}^{-1}$  while Fig. 4(b) shows that of  $Q = 1000 \text{ s}^{-2}$ . It has been pointed out that the vortex core boundaries based on  $|\omega|$ -definition are ambiguous while the  $Q$ -criterion is a proposed method to identify coherent vortex structures [21, 22]. And the comparison between two criterions in the present study clearly demonstrates that the  $Q$ -criterion is more suitable for vortex identification in the cases of flow past a circular cylinder. So, the  $Q$ -criterion is mainly used in the following discussion.

### 3. RESULTS AND DISCUSSION

Numerical simulations were carried out to investigate the effects of the end plate and yaw angle on the flow behavior. The scenario is quite different from that of the orthogonal cross flow towards a cylinder.

#### 3.1. Wake Vortex Structure

Fig. 5 shows a comparison of flow past a yawed circular cylinder at  $\alpha = 30^\circ$  between the present LES results and the experimental results by Matsuzaki et al. [23]. In fact, Fig. 5(a, b) can be seen as the vortex structures of flow past an infinite yawed circular cylinder as  $A$  is 30 for Fig. 5(a) and  $+\infty$  for Fig. 5(b), while Fig. 5(c, d) can be seen as the corresponding finite cases as  $A$  is 10 for Fig. 5(c) and 9 for Fig. 5(d).

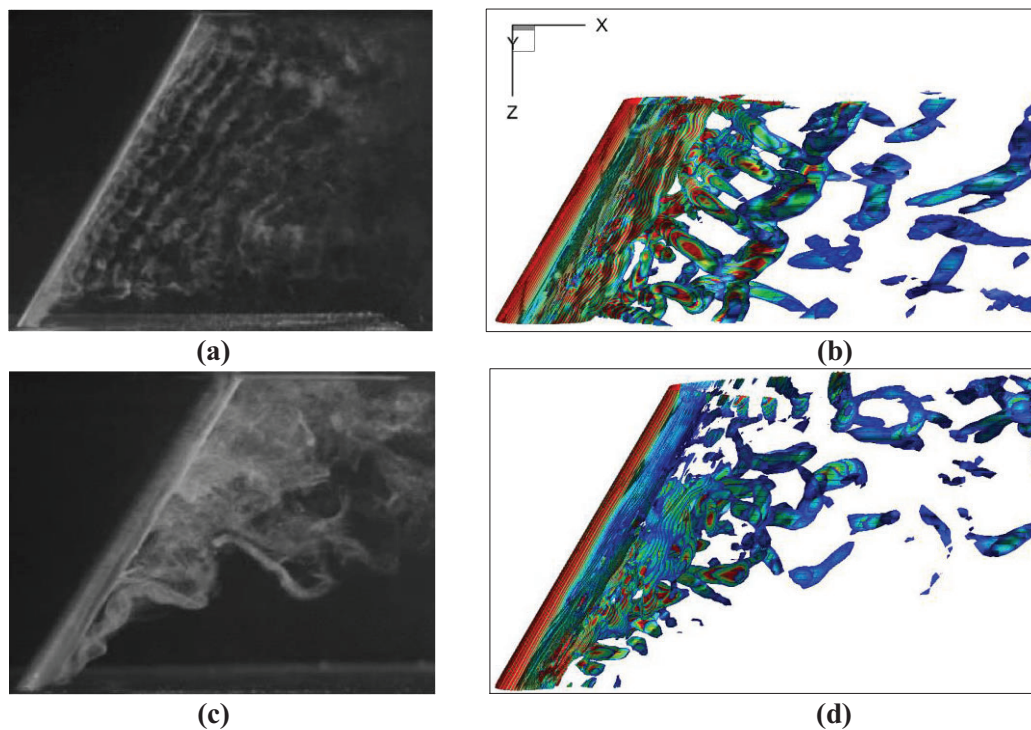


**Figure 5. Comparison of vortex structure at  $\alpha = 30^\circ$ : (a) experiment, Matsuzaki,  $A = 30$ ; (b) LES, present,  $A = +\infty$ ,  $Q > 750 \text{ s}^{-2}$ ; (c) experiment, Matsuzaki,  $A = 10$ ; (d) LES, present,  $A = 9$ ,  $Q > 750 \text{ s}^{-2}$ .**

As shown in Fig. 5(a, b), the axis of Karman vortex is parallel to the cylinder axis in the region where the influence of end plates can be ignored, which could be interpreted with IP. However, it can be seen from Fig. 5(c, d) that the Karman vortex street is broken down and there exists heaving upward flow along the cylinder axis when  $A = 9$  or 10. It has been reported that the axial flow or secondary flow along the cylinder axis [24-29], which flows upward from the upstream plate to the downstream plate in the present

study, is formed behind the circular cylinder. The interference of the axial flow with the end plates heavily influences the wake structure and the regular Karman vortex street cannot be observed when  $A < 10$ .

Fig. 6 illustrates the effect of yaw angle on the flow characteristics. In the finite cases as shown in Fig. 6(a), the traditional Karman vortex street can be still observed when  $\alpha = 15^\circ$ ; however, the regular Karman vortex street is broken down at  $\alpha = 30^\circ$  and  $45^\circ$ , which is owing to the interference of the axial flow with the end plates as mentioned above. This kind of phenomena does not emerge in the infinite cases and the traditional shedding of Karman Vortex Street can be clearly observed just as IP predicted (see Fig. 6(b)).

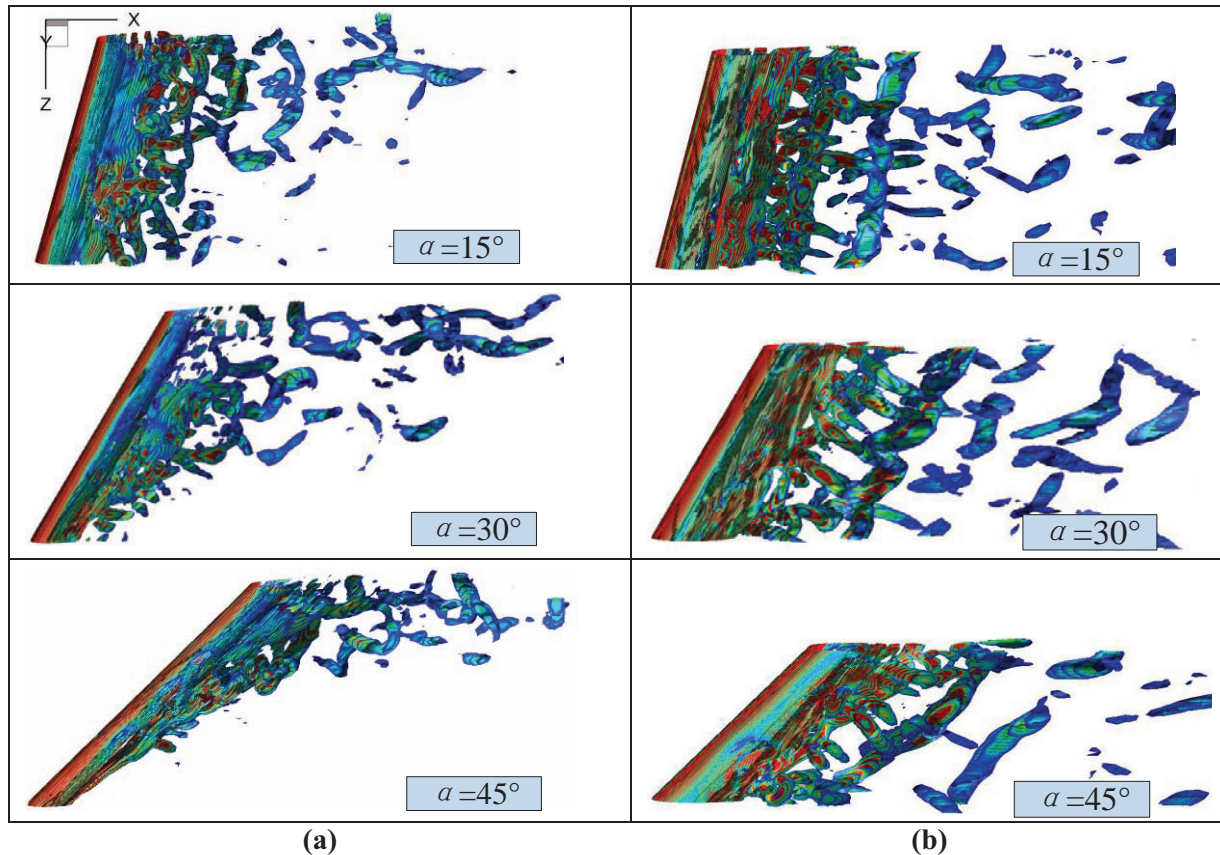


Figure 6. Comparison of vortex structure at different yaw angle,  $Q > 750 \text{ s}^{-2}$ : (a)  $A = 9$ ; (b)  $A = +\infty$ .

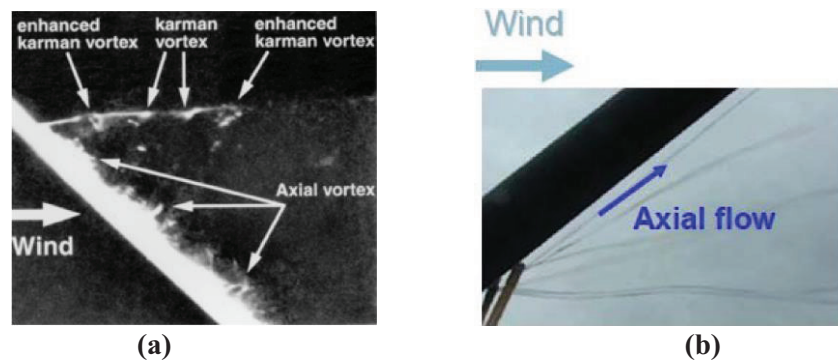


Figure 7. Visualized axial flow along the cylinder axis at  $\alpha = 45^\circ$  (Experiments of Matsumoto).

To visualize the axial flow, Matsumoto et al. [26-28] conducted different experiments and the results are shown in Fig. 7. It can be seen that the axial vortex is shedding from the rear part of the cylinder surface and the flow direction is mainly from the upstream plate to the downstream plate along the cylinder axis.

In the present simulation, the axial flow is also observed. Fig. 8 shows the evolution of instantaneous vortex structures seen from different perspectives at four continuous time series of  $t = 15.00\text{ s}$ ,  $15.05\text{ s}$ ,  $15.10\text{ s}$ , and  $15.15\text{ s}$  (from up to down).

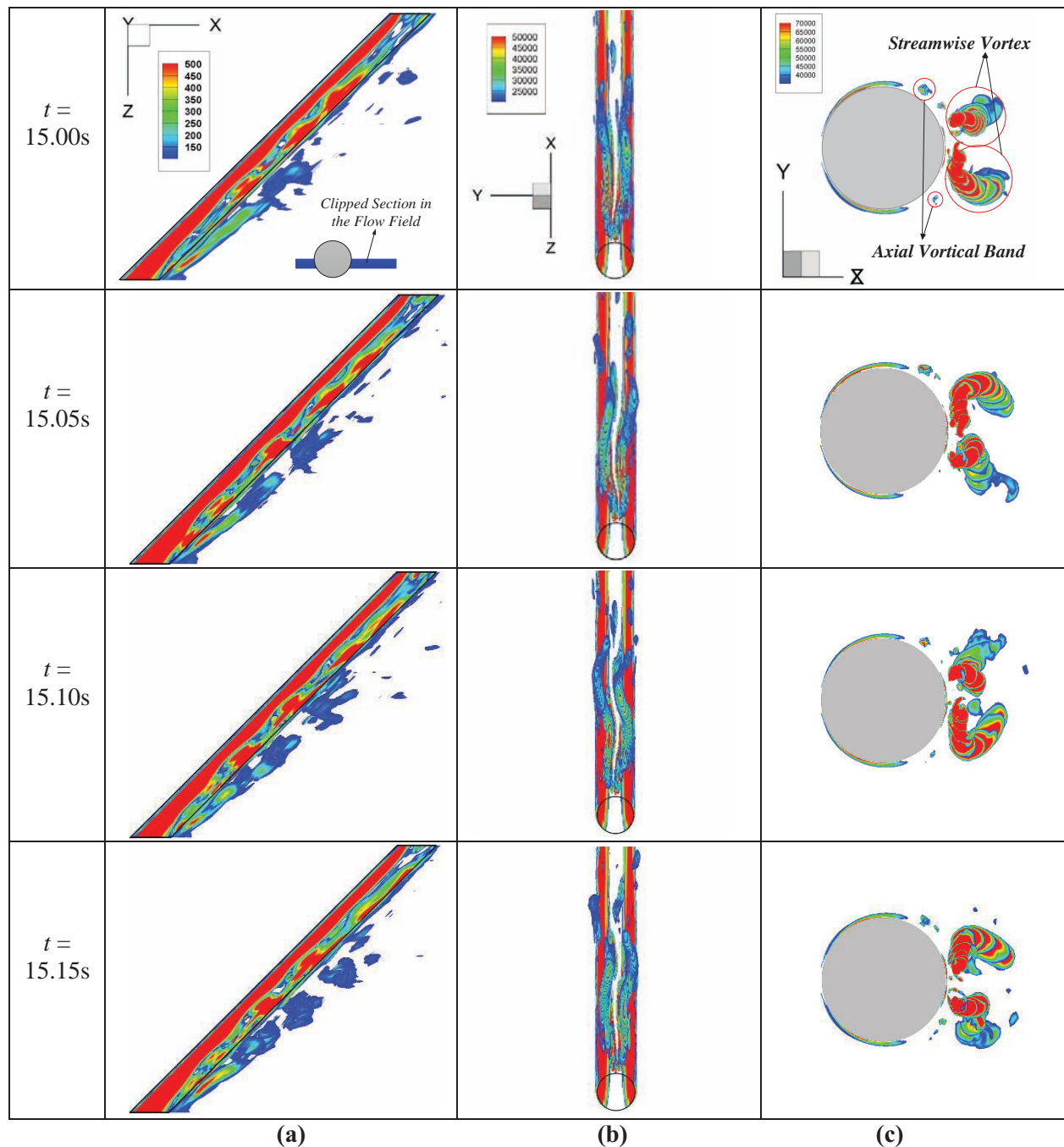


Figure 8. Simulated axial flow along the cylinder axis at  $\alpha = 45^\circ$  and  $A = 9$ : (a)  $100\text{ s}^{-1} < |\omega_{xy}| < 500\text{ s}^{-1}$ ; (b)  $20000\text{ s}^{-2} < Q < 50000\text{ s}^{-2}$ ; (c)  $35000\text{ s}^{-2} < Q < 70000\text{ s}^{-2}$ .

Fig. 8(a) shows the contours of  $|\omega_{xy}|$  between  $100 \text{ s}^{-1}$  and  $500 \text{ s}^{-1}$  at the clipped section shown in the first picture. It can be seen that there do exist axial flow and vortex-shedding along the cylinder axis. The axial flow is formed due to the balance results of normal component convection and the rear pressure distribution: the axial boundary layer parallel to the cylinder axis is pushed by the normal velocity and concentrated on the two flanks along the rear generatrix of the cylinder; the pressure in the lower region of rear generatrix varies along the backward stagnation line. And the axial flow is driven by the normal velocity component and shedding from the cylinder surface at a certain point where the pressure is lower than its surroundings.

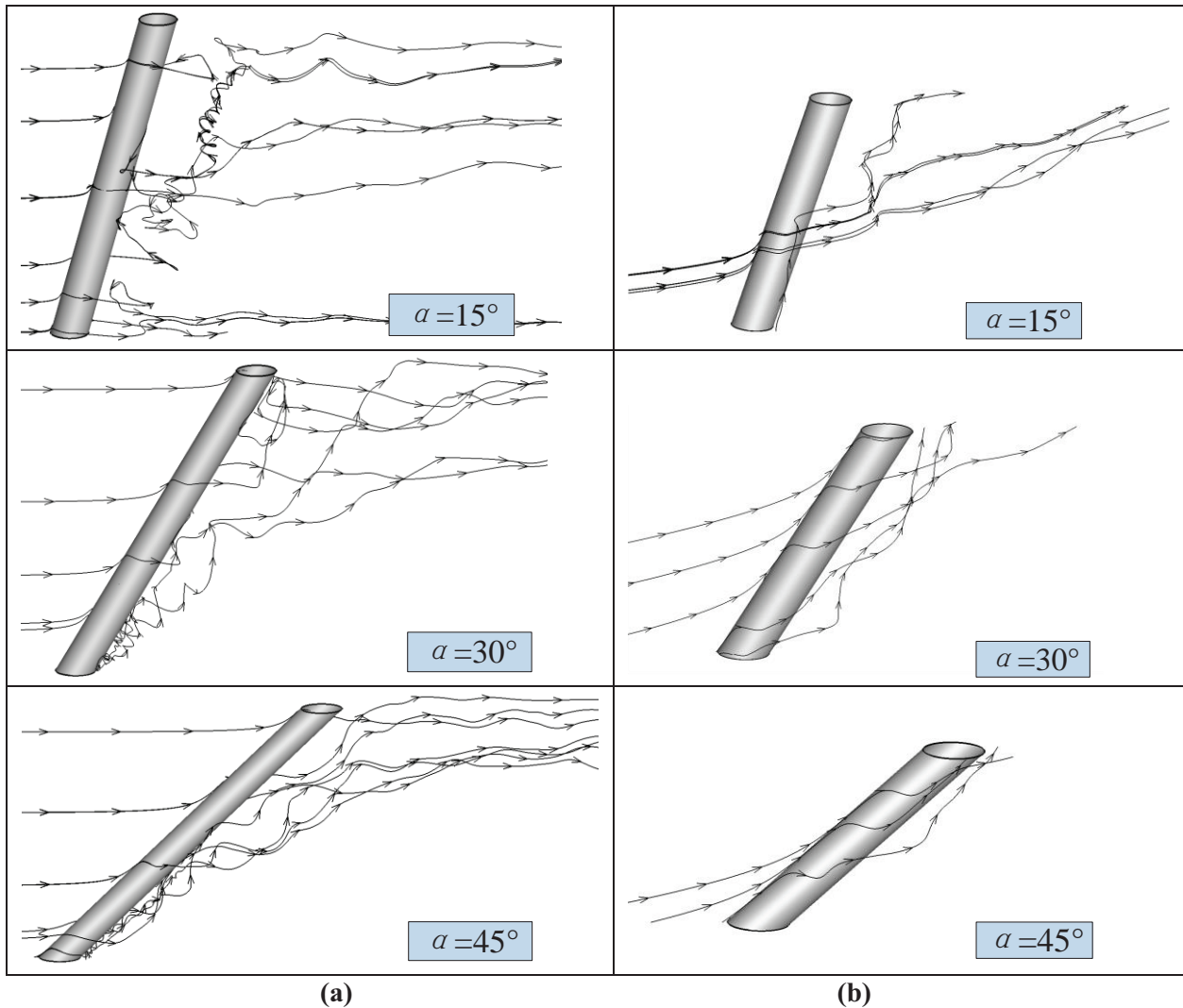
Fig. 8(b) shows the contours of  $Q$  seen from the opposite direction to the incoming velocity. It can be seen that the streamwise vortex is shedding as band structures on the both left and right sides on the rear part of the cylinder surface. They are originated from the intersection of the upstream plate and the backward stagnation line and spread towards the downstream plate. The two bands are almost symmetrical with the rear stagnant generatrix and shed simultaneously in the similar shape, the feature of which is different from the shedding behavior of the streamwise von Karman vortex street, in which the vortex is shedding alternatively from the left and right sides of the cylinder.

Fig. 8(c) shows the contours of  $Q$  seen along the cylinder axis from the upstream plate to downstream plate. It shows that the wake vortices are shed away out of the cylindrical surface respectively along two directions: one is abovementioned streamwise vortices with large strength, and another is axial vortices with small strength. The streamwise vortices (see Fig. 8(c)), with high strength, are obviously shedding from the lower rear part of the cylinder surface. They are concentrated and advected by the normal component of velocity towards the downstream plate. The vortices, attached to the cylindrical surface, are floated up along the axial direction, and then smoothly bent at the interaction of cylinder and downstream plate. At last they are convected downstream adhering to the wall of downstream plate. So a high shear flow is formed on the downstream plate, and uniform flow structure upstream of cylinder is transformed into the flow with highly uneven distribution of vortex. Meanwhile, two narrow axial vortical bands (see Fig. 8(c)) are also observed at the wake with small strength and size, which are situated at the positions that are a bit deviated from the two upright generatrices and earlier than the shedding points of the abovementioned streamwise vortices. It is shown from figures that they are evolved from the boundary shear layer and peeled at certain position and transformed into free vortices, and further developed into separate vortex clouds.

### 3.2. Streamlines

Fig. 9 shows the instantaneous streamlines at different yaw angle for both  $A = 9$  and  $A = +\infty$  cases. It can be seen that the axial flow is generated at both the front surface and rear surface, including the front stagnation line and the rear stagnation line for all yawed cases.

When a flow approaches the cylinder of finite length, the streamlines that approach the front leading edge of the cylinder are deflected towards the downstream plate. As the streamlines crosses the surface of the cylinder, the streamlines bend to the cross cylinder direction after they slide some distance along the spanwise direction. When the streamlines are crossed a bit beyond the upright ridges, they are again deflected to the downstream plate. After passing the cylinder, some streamlines near the upstream plate are trapped into the principal streamwise vortex and move in the spanwise direction in helical tracks, which are more obvious in the finite cases. Due to the upward flow along the cylinder axis for the finite cases, the flow is pushed and compressed at the corner formed by the cylinder and downstream plate and induced increased mixing of the mainstream flow behind the cylinder. This phenomenon is not observed in the infinite cases as the periodic boundary condition at two cylinder ends is employed so that flow can come into and out of the computational domain through two end plates (see Fig. 9(b)).



**Figure 9. Instantaneous streamlines at different yaw angle for both finite and infinite cases: (a)  $A = 9$ ; (b)  $A = +\infty$ .**

### 3.3. Spanwise Variation of Circumferential Pressure Profile

To further investigate the intrinsic mechanism of the generation of the secondary axial wall-attached flow on the rear wall of the cylinder, pressure distributions on 9 span-wise equally-spaced circumferential rings in the wall are taken out from the numerical simulation results for the two types of boundary conditions on the two lateral end-plates at three yaw angles. And here we take the cases at  $\alpha = 45^\circ$  as an example. As shown in Fig. 10(a), coefficients of the nine circular rings from the downstream plate to the upstream plate show a decrease in mean pressure in the angular region between  $\theta = 0^\circ$  and separation angle and an increase between the separation angle and  $\theta = 130^\circ$ . The morphology of the azimuthal surface pressure distribution at different sections along the cylinder axis could be spanwise grouped into three regions, i.e. the midspan region, the regions near two end plates. In the midspan region, as shown in circular rings 2 to 5, the pressure distributions are with similar shape and almost in agreement with each other, which are the same as the case of circular cylinder perpendicular to a uniform flow. So it demonstrates that quasi-two-dimensional flow behavior are held and the IP is still valid in this region. However, the surface pressure distributions in the regions near the two side end plates manifest themselves without similarity to that of

the midspan region, in which the flow near walls are obviously interfered with the wall effect. So the secondary axial flow should be engendered and thus the flows present three dimensional behavior and the IP is not valid in the two side regions.

Meanwhile, the surface pressure distribution in the two side wall regions are noticeably distinguished between each other. It is demonstrated that there exists different interference mechanisms between the effect of the cylinder inclination on flow and that of the wall effect on flow for the upstream plate and the downstream plate. In the side of downstream plate, its pressure distribution is not much different in shape from that of the midspan part, except for its earlier local minimum pressure point, which reveals the position of boundary shear layer separation. In the side of upstream end plate, two marked points in the curve should be mentioned. The first point in the curve is the local minimum point around at  $90^\circ$ , which is more retarded than those of the midspan and near downstream wall regions. That means the separation line on the surface of cylinder should be curved from the upright vertical position in the upstream end to some point in the front face in the downstream end (see Fig. 11(b)). The second point is the cusp formed in the trailing edge. We believe this is why the horseshoe vortex is formed in this region where the higher pressure prevents the wake vortex rolling up.

For the infinite cases, it can be seen from Fig. 10(b) that the pressure coefficients at different cross section along the cylinder axis are almost the same, which demonstrates that the end plate has a significant influence on the pressure distribution along the cylinder axis when  $A \leq 9$ .

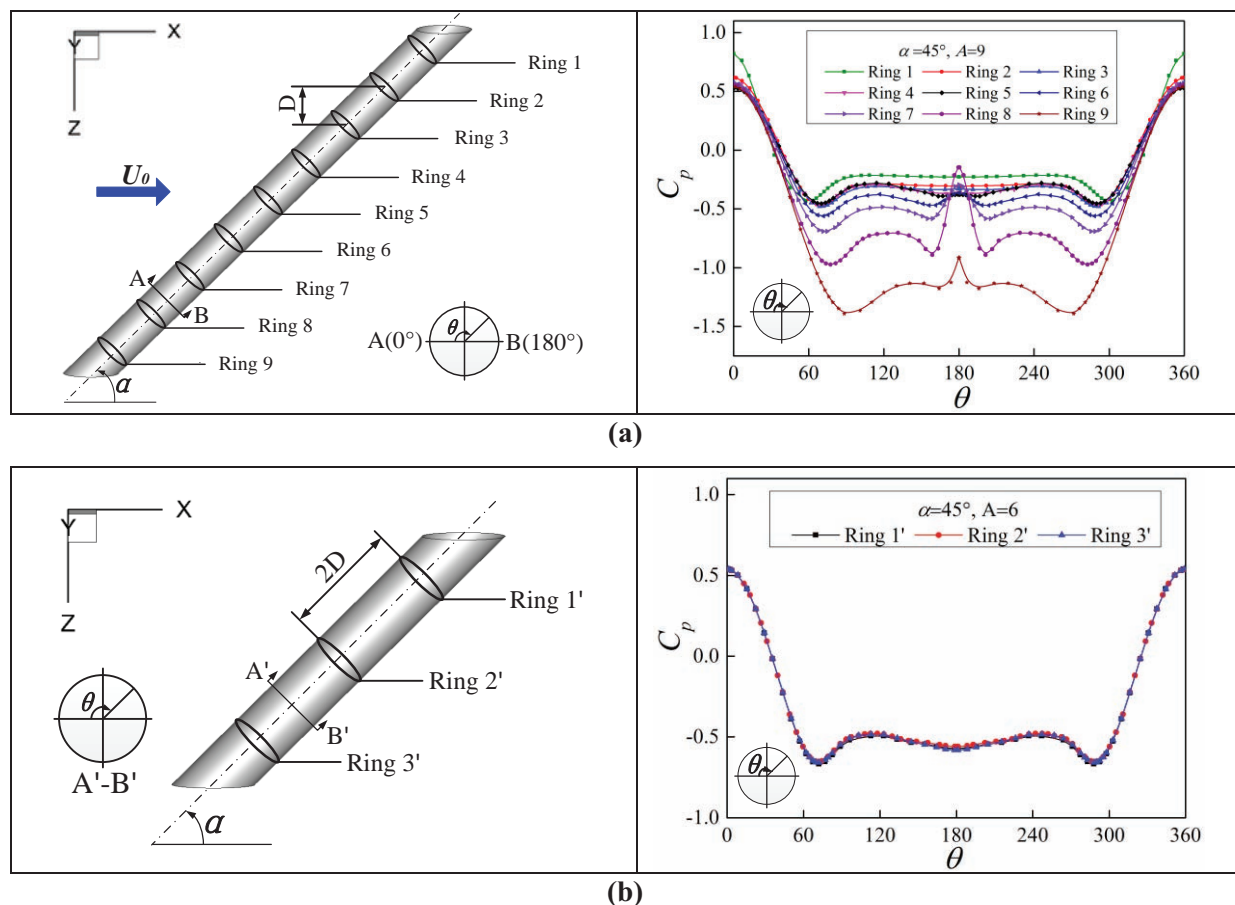
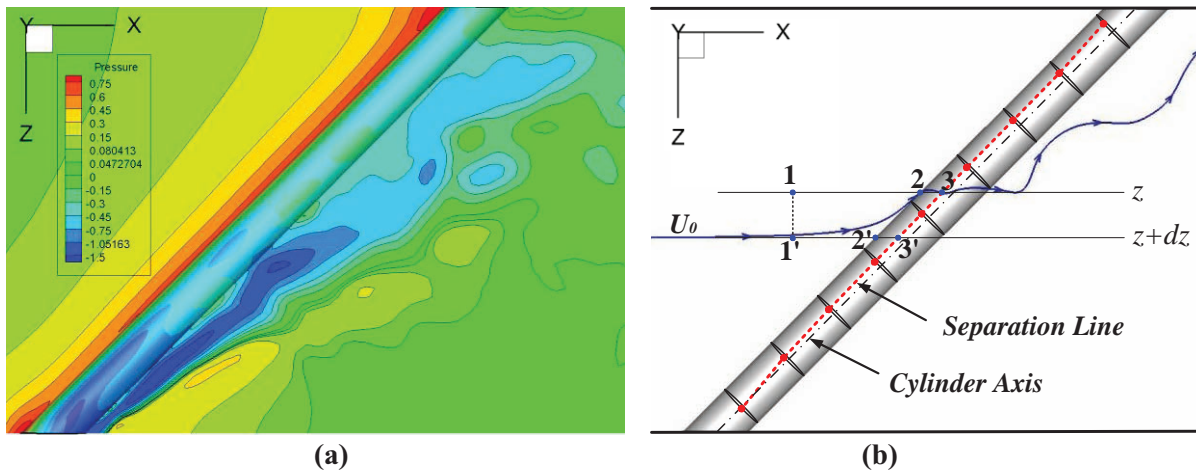


Figure 10. Comparison of pressure distribution at different cross section along the cylinder axis at  $\alpha = 45^\circ$ : (a)  $A = 9$ ; (b)  $A = +\infty$ .

Fig. 11(a) shows the instantaneous pressure distribution at the plane of  $y = 0$  when  $A = 9$  and  $\alpha = 45^\circ$ , and it can be used to analyze why the streamwise flow is skewed as shown in Fig. 9. Three regions divided according to the streamlines are considered: the region between  $x = 1$  (or  $1'$ ) and  $x = 2$  (or  $2'$ ), the region between  $x = 2$  (or  $2'$ ) and  $x = 3$  (or  $3'$ ), and the separation line. In the first region, the pressure acts towards the downstream plate, i.e.,  $dp/dz > 0$ ; so the main streamwise flow skewed toward the downstream plate. In the second region from the front leading edge to the separation line, the pressure shows a decrease and the pressure gradient is negative, i.e.,  $dp/dz < 0$ . This results in that the streamline bends back almost to the original direction and even becomes perpendicular to the cylinder axis. And for the separation line, the pressure gradient is zero, i.e.,  $dp/dz = 0$ . It is just at these positions that the boundary shear layers peeled from cylinder surface and transformed into free vortices.



**Figure 11. Analysis of the skewed streamwise flow at  $A=9$  and  $\alpha = 45^\circ$ : (a) Pressure distribution at the plane of  $y = 0$ ; (b) Analytical sketch of the skewed streamlines**

### 3.4. Strouhal Number

Here we check whether the principle of independence still holds or not in the cases of finite and infinite spanwise length cases. Fig. 12 shows the comparison of the computed  $Str$  in the present study with the experimental data obtained by Matsuzaki [23].

In Fig. 12, the results of present LES at  $A = 9$  and experimental data at  $A = 10$  agree with each other quite well when  $\alpha < 25^\circ$ , while the results of present infinite cases as well as previously reported experimental data for  $A = 30$  are in very good agreement with each other even at  $\alpha = 45^\circ$ . It also easy to find that the discrepancy between present LES at  $A = 9$  and IP becomes bigger and bigger with the inclination of yaw angle. But when  $A = +\infty$ , this kind of discrepancy can be neglected for free of the end wall effect.

Based on the dominant vortex shedding frequency, it was found that the  $Str_N$ , which is normalized by  $U_0 \cos \alpha$ , for  $\alpha = 15^\circ, 30^\circ$  and  $45^\circ$  are 0.2075, 0.1674 and 0.0968 when  $A = 9$ . The relative error are 3.41%, 22.08% and 54.96% respectively. This means that the IP cannot be used when  $\alpha > 30^\circ$  for the increased departure. But when  $A = +\infty$ , the  $Str_N$  are 0.2128, 0.2012 and 0.2051 and the relative error are 0.98%, 6.37% and 4.55% respectively, which means that the results of infinite cases support the IP even for  $\alpha = 45^\circ$ . For yaw angles smaller than  $45^\circ$ , the  $Str$  was well-corrected by using the component of the free-stream velocity that is orthogonal to the cylinder axis. Hence, for the  $Str$ , the IP was valid for the infinite cases.

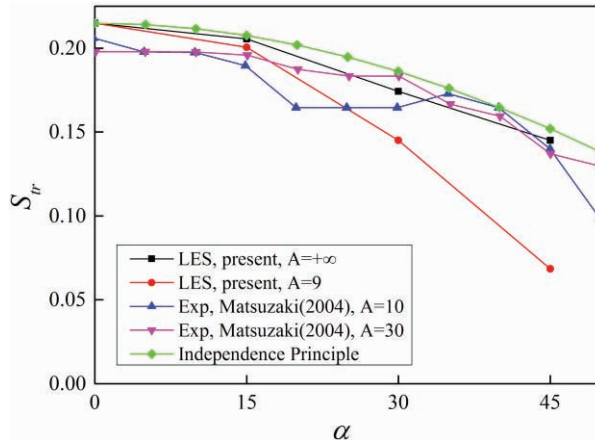


Figure 12. Effect of yaw angle on Strouhal number  $Str$ .

#### 4. CONCLUSIONS

The present simulations investigate the flow over a yawed circular cylinder at  $Re$  of 3900 using large eddy simulation. Four different yaw angle conditions are studied at both  $A = 9$  and  $+\infty$ , i.e.  $\alpha = 0^\circ, 15^\circ, 30^\circ$  and  $45^\circ$ . The effects of yaw angle and end plate on the flow behavior are discussed.

The effect of yaw angle on flow behavior is obvious especially for the finite cases. When  $A = 9$ , the regular Karman vortex street cannot be observed when  $\alpha > 30^\circ$  and there exists heaving upward flow along the cylinder axis. It shows that the wake vortices shed away out of the cylindrical surface along two directions: streamwise vortices and axial vortices. The former with high strength are obviously shedding from the lower rear part of the cylinder surface while the latter with small strength are situated at the positions that are a bit deviated from the two upright generatrices and earlier than the shedding points of streamwise vortices. From the results of streamlines, the helical tracks along cylinder axis are observed in the yawed cases. The discrepancy of  $Str$  between present LES at  $A = 9$  and predicted by IP becomes bigger and bigger with the increase of yaw angle. But when  $A = +\infty$ , this kind of discrepancy was not that apparent for free of the end wall effect.

The effect of end plate is studied by employing both free-slip and periodic boundary conditions at two end plates of the cylinder. It was found that the wake vortex structure, streamlines and pressure distribution along the cylinder span approach a highly quasi-two-dimensional state at  $A = +\infty$  with yaw angles up to  $45^\circ$ . Significant differences can be found for the flow at  $A = 9$ , in which cases the free-slip boundary condition at two side end-plates is employed so that the flow cannot come into and out of the computational domain through the two end plates. Thus the regular Karman vortex street is broken down and the flow is pushed and compressed at the corner formed by the cylinder and downstream plate especially when  $\alpha > 30^\circ$ . From the discussion of pressure distribution, the morphology of the azimuthal surface pressure distribution at different section along the cylinder axis was spanwise grouped into three regions, i.e. the midspan region, the regions near two end plates. In the midspan region, the quasi-two-dimensional state are held and the IP is still valid, while in the two side regions the secondary axial flow was engendered and thus the flows present three dimensional behavior and the IP is not valid. And the separation line on the surface of cylinder was curved from the upright vertical position in the upstream cylinder end to some point in the front face in the downstream cylinder end due to the interference of end walls. In general, the flow past a yawed cylinder follows the IP up to  $\alpha = 45^\circ$  in infinite cases but just about  $30^\circ$  when  $A = 9$ .

## NOMENCLATURE

In the present study, some variables like the drag coefficient  $C_D$ , lift coefficient  $C_L$ , pressure coefficient  $C_p$ , normalized pressure coefficient  $C_{p0}$ , aspect ratio  $A$  and non-dimensional time  $T^*$  are defined as follows:

$$C_D = F_D / (\rho D L U_0^2 / 2), C_L = F_L / (\rho D L U_0^2 / 2), C_p = (p - p_0) / (\rho U_0^2 / 2), C_{p0} = (p - p_s) / (\rho U_0^2 / 2), \\ A = L/D, T^* = U_0 t / D$$

where  $F_D$  is the drag force and  $F_L$  is the lift force acting on the cylinder,  $L$  is the spanwise length along  $z$ -direction,  $p$  is the pressure at the local flow field,  $p_0$  is the pressure at the far field,  $p_s$  is the pressure at the forward stagnation point and  $t$  is the physical flow time.

## ACKNOWLEDGMENTS

The authors would like to acknowledge the supports from the Science Fund for Creative Research Groups of National Natural Science Foundation of China (Grant No. 51321002).

## REFERENCES

1. Duan, Ri-Qiang and Sheng-Yao Jiang. "Numerical investigation of gas flow distribution and thermal mixing in helically coiled tube bundle," *Journal of Nuclear Science and Technology*, **45**(7), pp. 704-711 (2008).
2. Ramberg, S. E. "The effects of yaw and finite length upon the vortex wakes of stationary and vibrating circular cylinders," *Journal of Fluid Mechanics*, **128**, pp. 81-107 (1983).
3. Thakur, A., X. Liu and J. S. Marshall. "Wake flow of single and multiple yawed cylinders," *Journal of fluids engineering*, **126**(5), pp. 861-870 (2004).
4. Hayashi, Tsutomu and Tetuya Kawamura. "Non-uniformity in a flow around a yawed circular cylinder," *Flow Measurement and Instrumentation*, **6**(1), pp. 33-39 (1995).
5. Hayashi, Tsutomu, et al. "End effect on a yawed circular cylinder in uniform flow," *Bluff-Body Wakes, Dynamics and Instabilities*. Springer Berlin Heidelberg, pp. 59-62 (1993).
6. Zhao, Ming, Liang Cheng and Tongming Zhou. "Direct numerical simulation of three-dimensional flow past a yawed circular cylinder of infinite length," *Journal of Fluids and Structures*, **25**(5), pp. 831-847 (2009).
7. Beaudan, Patrick and Parviz Moin. *Numerical experiments on the flow past a circular cylinder at sub-critical Reynolds number*. No. TF-62. STANFORD UNIV CA THERMOSCIENCES DIV, 1994.
8. Breuer, Michael. "Numerical and modeling influences on large eddy simulations for the flow past a circular cylinder," *International Journal of Heat and Fluid Flow*, **19**(5), pp. 512-521 (1998).
9. Kravchenko, Arthur G. and Parviz Moin. "Numerical studies of flow over a circular cylinder at  $Re_D=3900$ ," *Physics of Fluids (1994-present)*, **12**(2), pp. 403-417 (2000).
10. Braza, M., P. H. H. M. Chassaing and H. Ha Minh. "Numerical study and physical analysis of the pressure and velocity fields in the near wake of a circular cylinder," *Journal of fluid mechanics*, **165**, pp. 79-130 (1986).
11. Niemann, H-J. and N. Hölscher. "A review of recent experiments on the flow past circular cylinders," *Journal of Wind Engineering and Industrial Aerodynamics*, **33**(1), pp. 197-209 (1990).
12. Norberg, Christoffer. "Effects of Reynolds number and a low-intensity freestream turbulence on the flow around a circular cylinder," *Chalmers University, Goteborg, Sweden, Technological Publications*, **87**(2) (1987).
13. Fröhlich, J., et al. "Large eddy simulation of flow around circular cylinders on structured and unstructured grids," *Numerical Flow Simulation I*, Springer Berlin Heidelberg, pp. 319-338 (1998).
14. Roshko, Anatol. "On the development of turbulent wakes from vortex streets," (1954).

15. Franke, J. and W. Frank. "Large eddy simulation of the flow past a circular cylinder at  $Re_D=3900$ ," *Journal of wind engineering and industrial aerodynamics*, **90**(10), pp. 1191-1206 (2002).
16. Kawamura, Tetuya and Tsutomu Hayashi. "Computation of Flow around a Yawed Circular Cylinder," *JSME International Journal Series B*, **37**(2), pp. 229-236 (1994).
17. Ong, L. and J. Wallace. "The velocity field of the turbulent very near wake of a circular cylinder," *Experiments in fluids*, **20**(6), pp. 441-453 (1996).
18. Lourenco, L. M. and C. Shih. "Characteristics of the plane turbulent near wake of a circular cylinder, a particle image velocimetry study," *private communication*, (1993).
19. Ma, X., G-S. Karamanos and G. E. Karniadakis. "Dynamics and low-dimensionality of a turbulent near wake," *Journal of Fluid Mechanics*, **410**, pp. 29-65 (2000).
20. Hunt, Julian CR, A. A. Wray and Parviz Moin. "Eddies, streams, and convergence zones in turbulent flows," (1988).
21. Jeong, Jinhee and Fazle Hussain. "On the identification of a vortex," *Journal of fluid mechanics*, **285**, pp. 69-94 (1995).
22. Wu, Jie-Zhi, Hui-Yang Ma and Ming-De Zhou. "Typical Vortex Solutions," *Vorticity and Vortex Dynamics*, Springer Berlin Heidelberg, pp. 255-321 (2006).
23. Matsuzaki, Kazuyoshi, et al. "Visualization of three-dimensional flow structures in the wake of an inclined circular cylinder," *Journal of Visualization*, **7**(4), pp. 309-316 (2004).
24. Kozakiewicz, Andrzej, J. Fredsøe and B. Mutlu Sumer. "Forces on pipelines in oblique attack: steady current and waves," *5th International Offshore and Polar Engineering Conference*, The Hague, The Netherlands, June 11-16, 1995, Vol. 2, pp. 174-183 (1995).
25. SHIRAKASHI, Masataka, Atsushi HASEGAWA and Shoichi WAKIYA. "Effect of the secondary flow on Karman vortex shedding from a yawed cylinder," *Bulletin of JSME*, **29**(250), pp. 1124-1128 (1986).
26. Matsumoto, M. "Vortex shedding of bluff bodies: a review," *Journal of Fluids and Structures*, **13**(7), pp. 791-811 (1999).
27. Matsumoto, Masaru, et al. "Vortex-induced cable vibration of cable-stayed bridges at high reduced wind velocity," *Journal of Wind Engineering and Industrial Aerodynamics*, **89**(7), pp. 633-647 (2001).
28. Matsumoto, Masaru. "The Role of Axial Flow in Near Wake on the Cross-Flow Vibration of the Inclined Cable of Cable-Stayed Bridges," *ASME 2010 3rd Joint US-European Fluids Engineering Summer Meeting collocated with 8th International Conference on Nanochannels, Microchannels, and Minichannels*, Montreal, Canada, August 1-5, 2010, pp. 1-9 (2010).
29. Choi, I. K., et al. "Endwall heat transfer and fluid flow around an inclined short cylinder," *International journal of heat and mass transfer*, **50**(5), pp. 919-930 (2007).